16. Ignacimuthu, S., Ribosomal DNA polymorphism in some pulses. *Indian J. Exp. Biol.*, 2000, **38**, 196–198.
17. Dellaporta, S. L., Wood, J. and Hick, J. B., A plant DNA minipreparation: version II. *Mol. Biol. Rep.*, 1983, **1**, 19–21.
18. Eckenrode, V. K., Arnold, J. and Meagher, R. B., Comparison of the nucleotide sequence of soybean 18S rRNA with the sequence of other small-subunit rRNAs. *J. Mol. Evol.*, 1985, **21**, 259–269.
19. Schiebel, K. and Hemleben, V., Nucleotide sequence of the 18S–25S spacer region from rDNA of mungbean. *Nucleic Acids Res.*, 1989, **17**, 2852.
20. Sambrook, J., Fritsch, E. F. and Maniatis, T., in *Molecular Cloning: A Laboratory Manual*, Cold Spring Harbor Laboratory Press, New York, 1989, 2nd edn.
21. Saini, A., Gopalakrishna, T., Reddy, K. S. and Jawali, N., The *Bam*HI site in the internal transcribed spacer region of mungbean ribosomal RNA gene is partially methylated. *Euphytica*, 2000, **144**, 55–59.
22. Chatterton, N. J., Hsiao, C., Asay, K. H., Jensen, K. B. and Wang, R. C., Nucleotide sequence of the internal transcribed spacer region of rDNA in the primitive oat species, *Avena longiglumis* Durieu (Gramineae). *Plant Mol. Biol.*, 1992, **20**, 163–164.
23. Volkov, R. A., Zanke, C., Panchuk, I. I. and Hemleben, V., Molecular evolution of 5S rDNA of *Solanum* species (Sect. Petota): application for molecular phylogeny and breeding. *Theor. Appl. Genet.*, 2001, **103**, 1273–1282.
24. Rafalski, J. A., Wiewiorowski, M. and Scoll, D., Organisation of ribosomal DNA in yellow lupine (*Lupinus luteus*) and sequence of the 5S RNA gene. *FEBS Lett.*, 1983, **152**, 241–246.
25. Arnheim, N., Concerted evolution of multigene families. in *Evolution of Genes and Proteins* (eds Nei, M. and Koehn, R. K.), Sinauer Associates Inc., Sunderland, Mass., 1983, pp. 38–61.
26. Hillis, D. M., Moritz, C., Porter, C. A. and Baker, R. J., Evidence for biased gene conversion in concerted evolution of ribosomal DNA. *Science*, 1991, **251**, 308–310.
27. Smartt, J., *Grain Legumes: Evolution and Genetic Resources*, Cambridge University Press, New York, 1990, pp. 140–175.
28. Doyle, J. J., 5S Ribosomal gene variation in the soybean and its progenitor. *Theor. Appl. Genet.*, 1988, **75**, 621–624.
29. Scoles, G. J., Gills, B. S., Xin, Z. Y., Clarke, B. C., Mc Intyre, C. L., Chapman, C. and Apples, R., Frequent duplication and deletion events in the 5S rRNA genes and the associated spacer regions of Triticeae. *Plant Syst. Evol.*, 1987, **160**, 105–122.
30. Menancio-Hautea, D., Fatokun, C. A., Kumar, L., Danesh, D. and Young, N. D., Comparative genome analysis of mungbean (*Vigna radiata* (L.) Wilczek) and cowpea (*Vigna unguiculata* (L.) Walpers) using RFLP mapping data. *Theor. Appl. Genet.*, 1993, **86**, 797–810.

Received 28 April 2003; revised accepted 18 June 2003

Equation-of-state study of copper using laser-induced shocks near 10 Mbar pressure and revalidation of theoretical modelling

M. Shukla[†,*], H. C. Pant[‡], V. K. Senecha[§], V. N. Rai[§], P. Khare[§§], A. K. Verma[†], R. S. Rao[†], N. K. Gupta[†] and B. K. Godwal[†]

[†]High Pressure Physics Division, Purnima Labs, Bhabha Atomic Research Centre, Trombay, Mumbai 400 085, India
[‡]Center for Advanced Technology, Indore 452 013, India
[§]Laser Plasma Division and [§§]Magnet Division, Center for Advanced Technology, Indore 452 013, India

Laser-driven shock wave experiments have been performed to determine equation of state (EOS) of copper using impedance matching technique in the pressure range 8–11 Mbar. A 2J/200 ps Nd : YAG laser beam is used to induce dynamic shocks in aluminium foil (reference material) and Al–Cu layered targets. EOS of copper is obtained at shock pressures of 8.9 Mbar and 10.4 Mbar with a pressure enhancement of ~ 1.66 at Al–Cu interface. The experimental data points are consistent with the predictions of the EOS model based on first principle theory and are also in close agreement with the simulation results obtained using one-dimensional radiation hydro-code MULTI that uses SESAME data tables for EOS and opacity values.

EQUATION-of-state (EOS) of a material at high pressures is an important input parameter for astrophysics, geophysics, inertial confinement fusion and hydrodynamic codes used for the simulation of fission, fusion devices. The EOS data up to 5 Mbar pressure is obtained with high explosive loading facility or using a high-pressure gas gun[1]. The pressure above 10 Mbar in the past had been obtained from underground nuclear explosions, but these measurements are difficult due to high cost and require large experimental configurations[2–4]. The efforts in the recent past reveal that laser-driven shock wave technique can be employed for achieving shock pressures of 10–40 Mbar within 15–20% accuracy in the laboratory conditions[5,6]. Recently, experiments using indirect drive method measures the shock pressure within an accuracy of 3–4% (ref. 7). With these developments it appears that laser-driven shocks can be used for the generation of accurate high-pressure data. These data can be utilized as a testing ground for the first principle theoretical models that is used for generating the EOS data in the pressure region not yet accessible experimentally. In this paper we present the extension of laser-driven shock wave experiments performed at CAT, Indore, to determine the EOS of copper (Cu) between 8 and 11 Mbar using impedance

*For correspondence.

matching technique. A 2J/200ps Nd : YAG laser beam is used to generate shocks in the planar Al foils and Al–Cu layered targets. The shock luminosity is recorded with a high speed S-20 streak camera. The experimental data obtained compares well with the numerical simulations performed using 1-dimensional radiation hydro-code MULTI on the shock pressure volume Hugoniot curve. This paper also presents the theoretical calculation of EOS of Cu that takes into account the contribution of first principle cold energy, thermal lattice vibrational and electronic excitation energies at various compressed volumes. The pressure as a function of compressed volume is found to be in agreement with the reported results of our experimental points as well as with the data from the other laboratories.

Having established the technique for EOS[8] measurement using laser-driven shock wave propagation in single and two layer targets, the aim of the present study is to extend it to another material copper for which data exist from other techniques above 10 Mbar pressures[9,10]. The suitability of first principle EOS calculations for generating the reliable data is checked for its use in theoretical simulations.

Figure 1 shows the schematic diagram of the experimental setup used to generate laser-induced shock in thin foil targets. A 2J/200ps laser beam with good spatial quality TEM_{00} output is used as a driver. The laser chain consists of a modified single shot commercial laser oscillator (Model PY61C-10) from M/s Continuum USA, External Pulse Selector (EPS), two silicate glass amplifiers and a Faraday isolator. The EPS based on avalanche transistor (2N5551) switching has been incorporated in the laser chain to increase the contrast ratio of the laser pulse to >5000 : 1 which otherwise is not suitable for laser-induced shock studies due to its poor contrast 50 : 1. A microprocessor-based control unit controls this MOPA chain. The laser beam is focused at incident intensity of $\sim 10^{14}$ watts/cm^2 on the 5 μm Al foil target and layered target consisting of 5 μm Al foil + 1 μm Cu kept in vacuum chamber evacuated to $\sim 10^{-3}$ torr. The shock luminosity signal at the rear surface of the target upon shock unloading is recorded with a high speed S-20 streak camera[11] with a temporal resolution of 5 ps as shown in Figure 1. A fiducial signal that serves as a marker for arrival of laser pulse on the target is also recorded each time the laser is fired on the target. This signal is generated by sampling part of the laser beam (~4%) and converting it to second harmonic before sending it through the optical fibre whose tip rests on the slit of the streak camera. The experimental technique is described in detail in ref. 8.

The shock velocity in pure Al foil of 5 μm (thickness variation ± 0.1 μm) used as the reference material is determined at absorbed laser intensities of 4.4×10^{13} and 3.8×10^{13} W/cm^2 as shown in Table 1. The corresponding particle velocity and pressure in Al is calculated as per Rankine–Hugoniot relations:

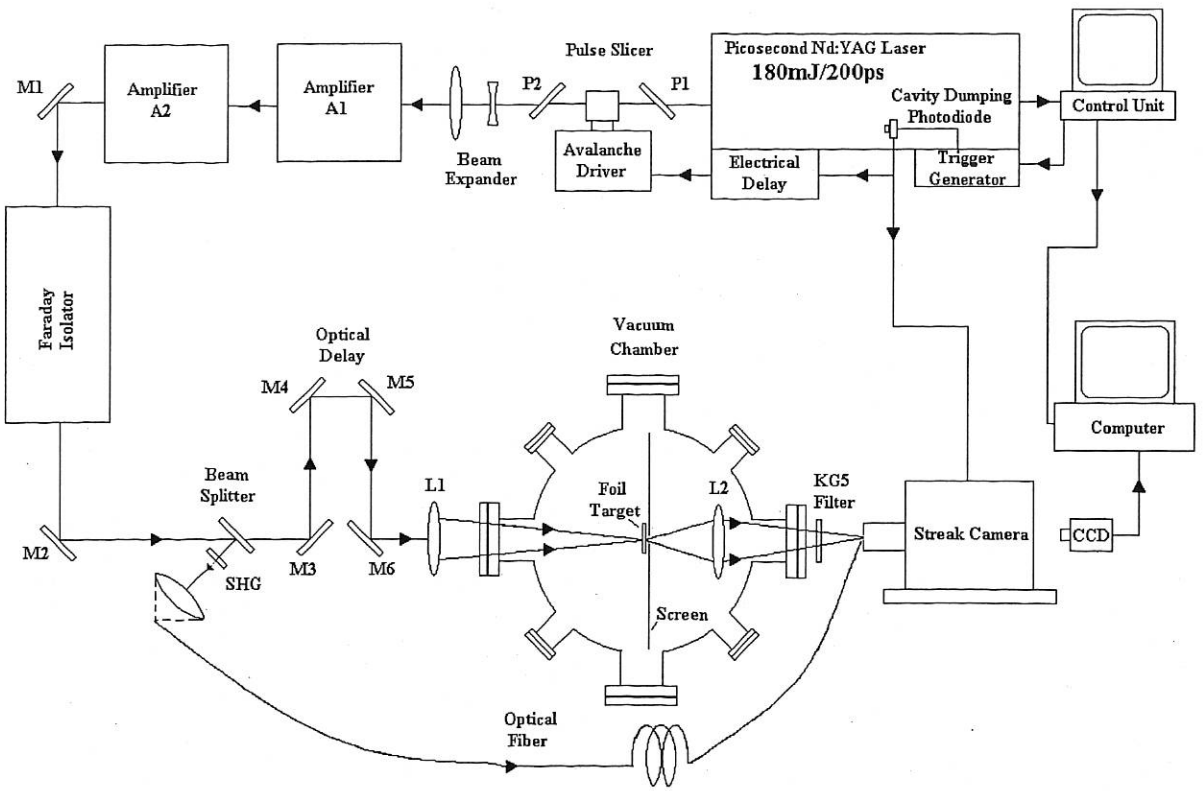

Figure 1. Experimental setup.

Table 1. Results of Al–Cu impedance match experiment

	Aluminium					Copper				
Absorbed laser intensity ~ ($\times 10^{13}$) Watts/cm^2	Target thickness	Shock transit time (ps)	Shock velocity ($\times 10^6$ cm/s) u_s(Al)	Particle velocity ($\times 10^6$cm/s) u_p(Al)†	Pressure (Mbar) P_1	Target thickness	Shock transit time (ps)	Shock velocity ($\times 10^6$ cm/s) u_s (Cu)*	Particle velocity ($\times 10^6$cm/s) u_p(Cu)	Pressure (Mbar) P_2
4.4	5 μm ± 0.1	243 ± 3.2	2.06 ± 0.05	1.13 ± 0.03	6.24 ± 0.30	1 μm ± 0.05	66 ± 3.2	1.54 ± 0.12	0.76 ± 0.05	10.38 ± 0.96
3.9	5 μm ± 0.1	257 ± 3.2	1.94 ± 0.04	1.04 ± 0.02	5.44 ± 0.25	1 μm ± 0.05	75 ± 3.2	1.45 ± 0.09	0.70 ± 0.04	8.90 ± 0.81

†u_s(Al) = 0.5386 + 1.339u_p(Al).
*u_s(Cu) = 0.3933 + 1.51u_p(Cu).
Pressure multiplication (m) ~ 1.66.

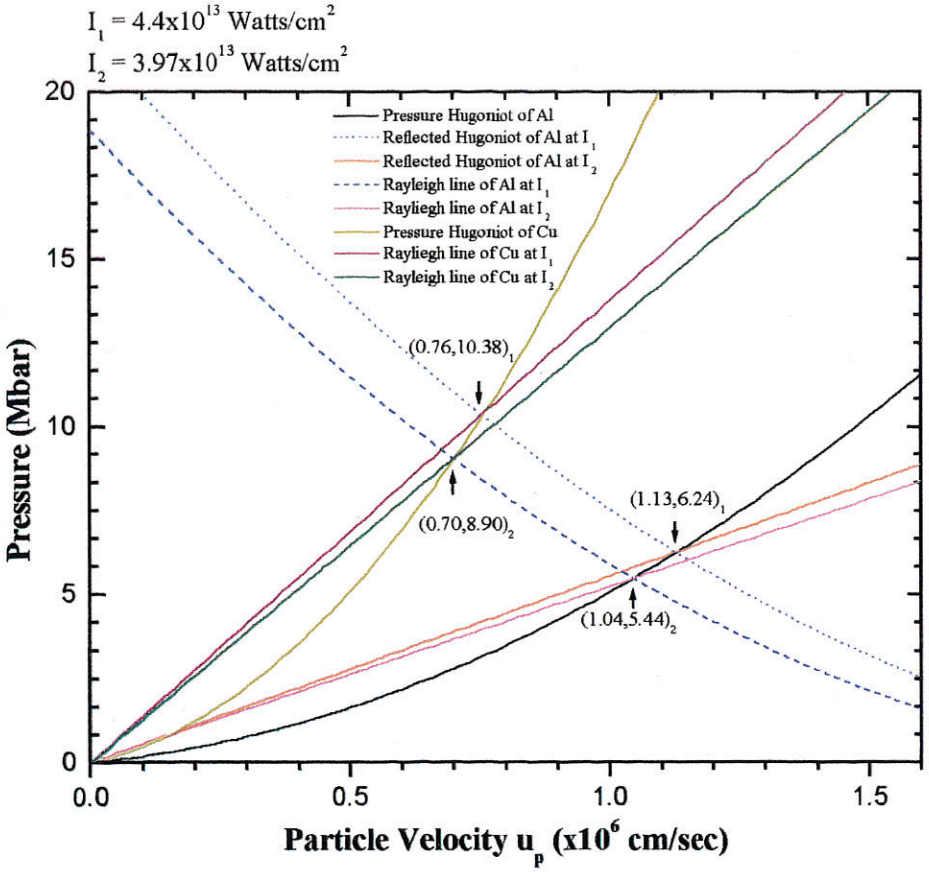

Figure 2. Hugoniot curve for Al + Cu layered target.

$$u_s = a + bu_p, \quad (1)$$

$$P = \rho_s u_s u_p, \quad (2)$$

where a and b are constants, u_s is the shock velocity (10^6 cm/s), u_p is the particle velocity (10^6 cm/s), ρ_s is the density (g/cc) of the material and P is the pressure (Mbar). For Al, $a = 0.5386$, $b = 1.339$ and $\rho_s = 2.7$g/cc and the shock pressure at the two absorbed laser intensities is found to be 6.24 and 5.44 Mbar respectively as shown in Figure 2, which represents the Hugoniot curve in P–u_p plane.

The layered target consisting of 5 μm Al foil + 1 μm Cu is used to determine the EOS of Cu using impedance matching technique. Copper is deposited on the rear surface of the foil using vacuum deposition technique. Suitable arrangement was made in the coating unit to achieve good adhesion between Al and Cu and to keep the thickness variation within ± 0.05 μm. Figure 3 *a*, *b* shows typical recorded shock luminosity signals in pure Al and Al–Cu layered target respectively. These luminosity signals were recorded at the same absorbed laser intensity. As shown in Figure 2 and represented in Table 1, the reflected Hugoniot curve of Al cuts the experimentally

determined Rayleigh lines of Cu at 10.38 Mbar and 8.90 Mbar on P–u_p plane for shock velocities of 1.54×10^6 cm/s and 1.45×10^6 cm/s respectively. For Cu; $a = 0.3933$, $b = 1.51$ and $\rho_s = 8.93$ g/cc. The pressure enhancement factor at the Al–Cu interface is found to be 1.66.

The values of $(a, b) = (0.3933, 1.50)$ as per eq. (1) is obtained by applying best linear fit to the experimental data as shown in Figure 4.

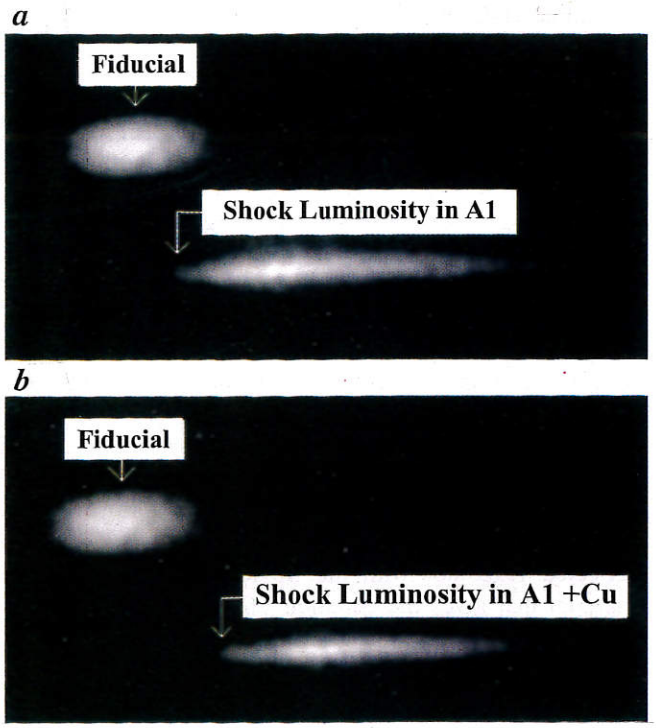

Figure 3. *a*, Shock luminosity signal in Al target; *b*, Shock luminosity signal in Al + Cu layered target.

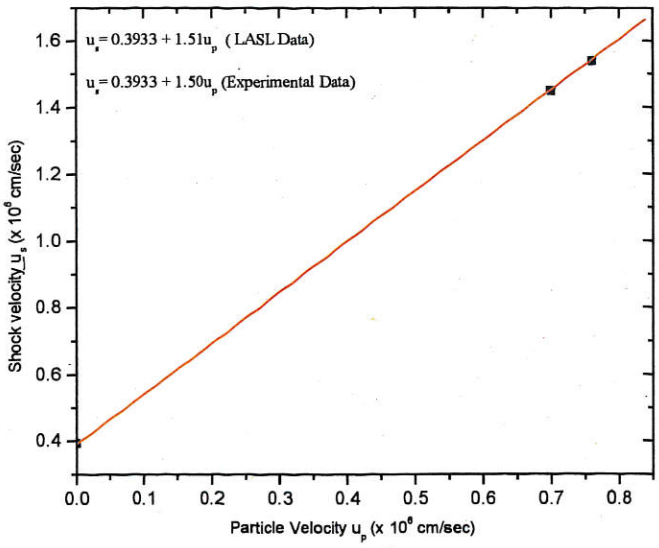

Figure 4. Experimentally obtained u_s–u_p relationship.

A proper radiation hydrodynamic simulation can serve as an important tool in predicting proper target thickness that can avoid the effects of preheating and also ensure steady state shock wave propagation conditions. The one dimensional (1-D) numerical simulation study using radiation hydro code MULTI[12] shows that for the experimental laser irradiation ($I = 10^{14}$ W/cm^2; $\lambda = 1.06$ μm; pulse FWHM = 200 ps), the base material must be thicker than 3.4 μm to reach stationary condition. The experiment was performed with varying Al foil thickness from 4–8 μm for measuring the shock velocity[8]. We also noticed that the shock wavefront as well as pressure profiles reaches a steady state condition at 250 ps after the start of the laser pulse and it continues in this state till it breaks out from the rear surface at 300 ps. We have also simulated Al–Cu targets for our experimental conditions where we find that the shock pressure gets enhanced by a factor of ~1.67 at the boundary of the two materials as represented in Figure 5.

The EOS of Cu was theoretically simulated by employing models[13] using the first principles energy band structure results. We calculate at various volumes the total energy, that is the sum of cold (absolute zero) energy, the thermal lattice vibrational and electronic excitation energies. The cold energy is calculated using all-electron full potential linear augmented plane wave (FP-LAPW) method as documented by Blaha *et al.*[14,15] with generalized gradient approximation (GGA) for exchange correlation[16]. The calculated equilibrium volume of 80.52 (in a.u.) per atom is about 1.15% larger than the measured value and the bulk modulus of 1.42 Mbar compares well with the experimental value of 1.40 Mbar. The calculated Grüneisen parameter is 2.12 as compared to the experimental value of 1.97 (ref. 17). This value of the bulk modulus was used to compute the Debye temperature to estimate the lattice thermal energies at various compressions by the

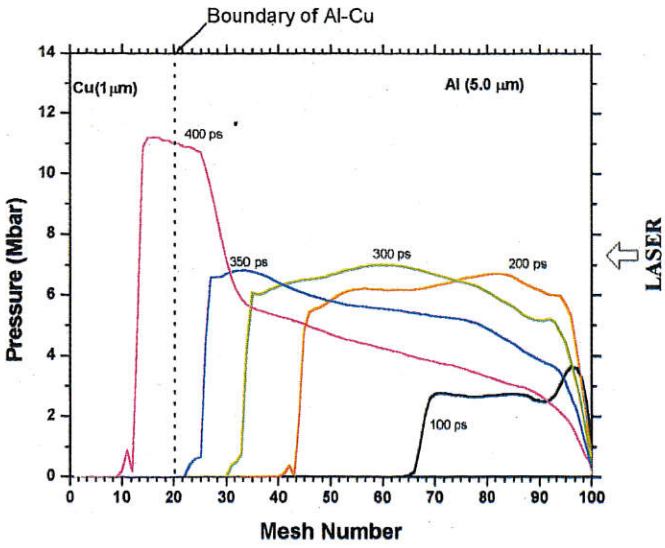

Figure 5. Pressure profiles for Al + Cu target.

Debye–Mie Grüneisen model[18]. This is based on the assumption that the vibrational energy levels of ions are the same as those of harmonic oscillators. Using the average lattice Grüneisen parameter, the corresponding contribution to pressure was estimated. The free electron Fermi–Dirac formulae using density of states at the Fermi level obtained by our FP-LAPW calculations were used to estimate the electronic thermal excitation energy and pressure. The electronic Grüneisen parameter (γ_e) needed for the calculation of pressure due to thermal electronic excitations was computed by using the electronic band structure results by employing the formula[19]

$$\gamma_e = [V/N(E_F)]/[dN(E_F)/dV], \quad (3)$$

where the density of electronic states, $N(E_F)$, at the Fermi level (E_F) at volume V is obtained from the calculated electronic bands at various compressions. The total energy and pressure at each volume as a function of temperature was used in Rankine–Hugoniot relations to obtain the Hugoniot pressure, volume and temperature self-consistently. The Lindeman law and dislocation-mediated melting formalisms were used to generate the melting curve[20,21]. We found that melting due to irreversible shock heating along the shock Hugoniot of Cu occurs at around 2.5 Mbar. It is thus natural that the liquid Hugoniot calculations should be used above the shock melting. However, it has been found that Hugoniot P–V curve in solid and liquid states are in mutual agreement within experimental error bars[13], hence all the calculations were carried out in solid state by neglecting the liquid disorder. Figure 6 depicts the comparison of the calculated room temperature isotherm with that of Nellis *et al.*[22]. In evaluating this isotherm we have also checked that Cu does not undergo a structural phase transition to other commonly occurring structures (*hcp*, *bcc*), which could change the isotherm at pressures higher than the transition pressure, especially in view of a similar high pressure transition predicted in gold[23]. Since the particle velocity and the compressed volume relation is

$$V/V_0 = 1-u_p/u_s, \quad (4)$$

where V is the final volume achieved after compression of the material by a shock wave and V_0 is the volume at the initial state; the pressure from eq. (2) can be written as a function of compressed volume as

$$\text{Pressure } P = \rho_0 u_s^2(1-V/V_0). \quad (5)$$

The simulated and experimental data on Hugoniot P–V curve along with those of other laboratories[25–29] are shown in Figure 7.

The laser-induced shock generation in thin metal targets for EOS studies aims at minimizing the possible errors that are introduced in the shock velocity, particle velocity and pressure. The impedance matching technique analysis involves: (a) Evaluation of EOS (P, ρ, E, u_s, u_p) point in the reference material from the measured shock velocity, (b) Construction of reflected pressure Hugoniot curve at the reference point of the shock reflected in the unknown material, (c) Intersection of the reflected Hugoniot with the Rayleigh line of unknown material that gives the common EOS point in P–u_p plan. Thus at the intersection point of reflected Hugoniot and the Rayleigh line, the error in pressure is quadrature and is given by

$$\Delta P/P = \sqrt{[(\Delta P_{ref}/P_{ref})^2 + (\Delta P_{unk}/P_{unk})^2]}, \quad (6)$$

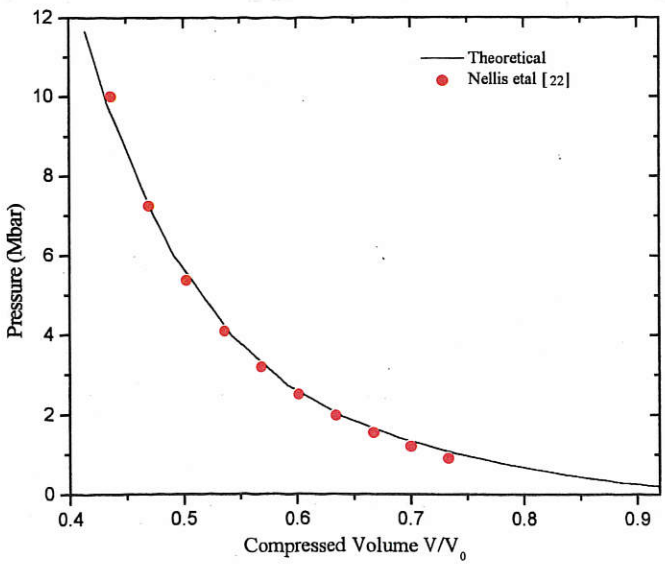

Figure 6. Room temperature isotherm curve.

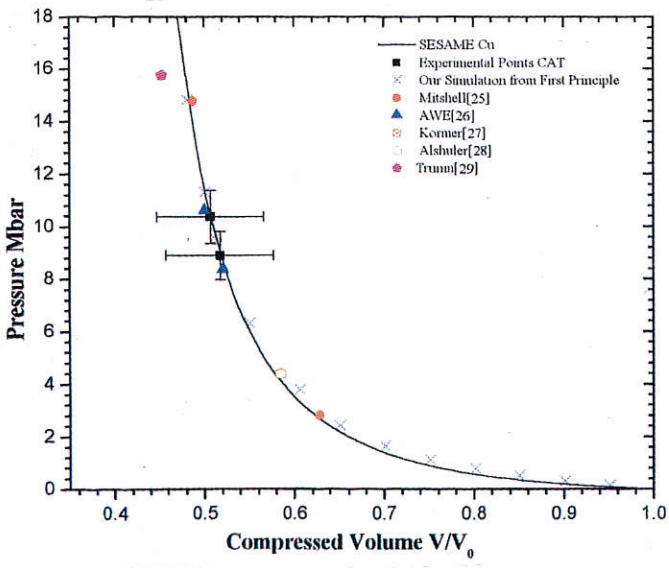

Figure 7. Pressure Hugoniot curve represented as pressure vs compressed volume.

where $\Delta P_{ref}/P_{ref}$ is the error in the reference material (Al) and $\Delta P_{unk}/P_{unk}$ is the error in the unknown material used (Cu). Since $P = \rho u_s u_p \alpha \rho u_s^2$ on a pressure Hugoniot curve and $P \alpha \rho u_s$ on a Rayleigh line, the eq. (6) leads to

$$\Delta P/P = \sqrt{[(\Delta\rho_0/\rho_0)^2_{ref} + 4(\Delta u_s/u_s)^2_{ref} + (\Delta\rho_0/\rho_0)^2_{unk} + (\Delta u_s/u_s)^2_{unk}]}. \quad (7)$$

Density error in Al is ignored since the foil (thickness variation ± 0.1 μm) was procured from a standard manufacturer. However the density of Cu normally achieved by the vacuum deposition technique is ~ 0.96 of the solid density[7]. Thus eq. (7) leads to

$$\Delta P/P = \sqrt{[4(\Delta u_s/u_s)^2_{ref} + (\Delta\rho_0/\rho_0)^2_{unk} + (\Delta u_s/u_s)^2_{unk}]}. \quad (8)$$

The fractional errors are assumed to be independent but it is equal for each step. The possible errors that contribute to the shock velocity are errors due to the foil thickness variation, transit time and streak camera calibration. Thus from eq. (7) the variation in shock velocity is

$$(\Delta u_s/u_s)^2_{ref\ or\ unk} = [(\Delta d/d)^2 + (\Delta t/t)^2_{transit} + (\Delta t/t)^2_{calib}], \quad (9)$$

where $\Delta d/d$ is the thickness variation error, $(\Delta t/t)_{transit}$ is the transit time error and $(\Delta t/t)_{calib}$ is the streak camera calibration error.

The variation in the coating thickness for vacuum deposition is given by

$$d_1/d_0 = [1 + (x/h)^2]^{-2}, \quad (10)$$

where d_0 is the deposited thickness at the centre and d_1 is deposited thickness at the target boundary of dimension 25.4 mm × 25.4 mm. In the coating unit $x = 12.7$ mm from the centre of the target whereas the height of the target from the source was $h = 100$ mm. Thus the deposited thickness has a variation of ± 0.05 μm for Cu. Streak camera used in our experiment has a temporal resolution of ~ 5 ps for the streak rate of 15.62 mm/ns. Therefore for streak camera calibration error $(\Delta t/t)_{calib}$ of ~ 0.3% and the transit time CCD pixel value of ~ 3.2 ps, the error in pressure for Al (reference) is calculated to be ~ ± 5% from the relation

$$(\Delta P/P)_{ref} = \sqrt{[4(\Delta u_s/u_s)^2_{ref}}, \quad (11)$$

whereas the error in pressure for Cu as per eq. (6) is ~± 9.3%. The calculated errors in shock velocity, particle velocity and pressure for Al and Cu are shown in Table 1.

The technique established earlier to determine the EOS of Au using impedance matching technique is used here to successfully determine the EOS of Cu between 8–11 Mbar pressure. The shock and particle velocities obtained in Al and Cu compare well with the reported results of SESAME[24]. The Hugoniot curve constructed for copper from experimental data also shows good agreement with the theoretical data available in LASL data book[30]. The value of (a, b) constants = (0.3933, 1.50) as per eq. (1) also compares well with the LASL data of (a, b) = (0.3933, 1.51). The simulation results obtained using first principle model calculations corroborates well with the experimental results. A pressure enhancement of ~1.67 predicted by the simulation results of one-dimensional radiation hydrocode MULTI also compares well with the experimentally obtained pressure enhancement value of ~1.66. From the error analysis we can say that our shock velocity measurement points are fairly in good agreement within the error limit of ± 2.4% for Al and ± 6.9% Cu. Thus our shock pressure values determined in the present experiment are correct within the errors of ± 5% for Al and ± 9.3% for Cu, using impedance matching technique. The direct drive method using optical smoothing technique such as random phase plate or phased zone plate produces a flat laser spatial profile. In the present experiment no attempt was made to achieve a flat shock profile. However, the optimum foil thickness of 5 μm for Al helped in minimizing the pre-heat effects due to hard X-rays[31]. Further the laser intensities are well within the limits beyond which hot electrons may also lead to pre-heat effect.

1. McQueen, R. G. *et al.*, *High Velocity Impact Phenomenon* (ed. Kinslow, R.), Academy Press, New York, 1970, p. 293.
2. Al'etshuler, V. *et al.*, *Sov. J. Appl. Mech. Tech. Phys.*, 1981, **22**, 145.
3. Ragan III, C. E., *Phys. Rev.*, 1982, **A25**, 3360.
4. Trunin, R. F. *et al.*, *Sov. Phys. JETP*, 1969, **29**, 630.
5. Van Kessel, C. G. M., *et al.*, *Phys. Rev. Lett.*, 1974, **33**, 1020.
6. Trainor, R. J., *et al.*, *Phys. Fluids*, 1982, **25**, 1989.
7. Rothman *et al.*, *Phys. Plasmas*, 2002, **9**, 1721.
8. Pant, H. C. *et al.*, *Curr. Sci.*, 2002, **82**, 149.
9. Benuzzi, A. *et al.*, *Phys. Rev.*, 1996, **E54**, 2162.
10. Gu, Y. *et al.*, *Laser Particle Beams*, 1996, **14**, 157.
11. Rai, V. N., Shukla, M., Pant, H. C. and Bhawalkar, D. D., *Sadhana*, 1995, **20**, 937.
12. Ramis, R. *et al.*, *Comput. Phys. Commun.*, 1988, **49**, 475.
13. Godwal, B. K., Sikka, S. K. and Chidambaram, R., *Phys. Rep.*, 1983, **102**, 121.
14. Blaha, P., Schwarz, K. and Dederichs, P. H., *Phys. Rev.*, 1988, **B37**, 2792.
15. Blaha, P., Schwarz, K., Sorantin, P. and Trickey, S. B., *Comput. Phys. Commun.*, 1990, **59**, 399.
16. Perdew, J. P., Burke, K. and Ernzerhof, M., *Phys. Rev. Lett.*, 1996, **77**, 3865.
17. Gschneidner, Jr K. A., in *Solid State Physics* (eds Seitz, F. and Turnbull, D.), Academic, New York, 1964, vol. 16, p. 275.
18. Kittel, C., *Introduction to Solid State Physics*, Wiley Eastern, New Delhi, 1993.
19. Godwal, B. K. and Raymond Jeanloz, *Phys. Rev.*, 1990, **B41**, 7440.
20. Burakovsky, L., Preston, D. L. and Silbar, R. R., *Phys. Rev.*, 1996, **B61**, 15011.
21. Zel'dovich, Ya. B. and Raizer, Yu. P., *Physics of Shock Waves and High Temperature Hydrodynamics Phenomena*, Academic Press, NY, 1976.

22. Nellis, W. J. *et al.*, *Phys. Rev. Lett.*, 1988, **60**, 1414.
23. Ahuja, R., Rekhi, S. and Johansson, B., *Phys. Rev.*, 2001, **B63**, 212101.
24. SESAME report on the Los Alamos Equation-of-state Library, LANL Report No. LALP-83-4, T-4 Group LANL, Los Alamos, 1983.
25. Mitchell, A. C. *et al.*, *J. Appl. Phys.*, 1991, **69**, 2981.
26. Evans, A. M., *et al.*, *Laser Particle Beams*, 1996, **14**, 113.
27. Kormer, S. B. *et al.*, *Sov. Phys. JETP*, 1962, **15**, 477.
28. Altshuler, L. V. *et al.*, *Sov. Phys. JETP*, 1962, **11**, 573.
29. Trunin, R. F. *et al.*, *Sov. Phys. JETP*, 1962, **29**, 630.
30. Marsh, S. P., *LASL Shock Hugoniot Data*, University of California Press, Berkeley, 1980.
31. Honrubia, J. J. *et al.*, *Advances in Laser Interaction with Matter and Inertial Fusion* (eds Velarde, G. *et al.*), World Scientific, Singapore, 1996, p. 34.

ACKNOWLEDGEMENTS. We acknowledge the encouragement and support received from Dr Anil Kakodkar. We are also extremely thankful to Dr S. K. Sikka, Dr D. D. Bhawalkar and Dr R. Chidambaram for their keen interest in the work and helpful discussions.

Received 17 February 2003; revised accepted 12 June 2003

Geochemistry of high-Mg mafic dykes from the Bastar craton: evidence of late Archaean boninite-like rocks in an intracratonic setting

Rajesh K. Srivastava* and R. K. Singh

Department of Geology, Igneous Petrology Laboratory, Banaras Hindu University, Varanasi 221 005, India

Mafic rocks of varying petrological and geochemical characteristics are exposed in the Bastar craton in the form of dykes as well as volcanics. Two sets of sub-alkaline mafic dyke swarms are well-recognized. The older set of sub-alkaline mafic dykes is middle Archaean, whereas the younger set is Palaeoproterozoic in age. In the present communication we report another set of mafic dyke swarms, which is also exposed in the southern part of the Bastar craton and has entirely different geochemical characteristics. This set of dyke swarms is intruded into granite gneisses and is late Archaean in age. Geochemically, these dykes contain high silica (> 52%) and magnesium (~ 12%) and low titanium (< 0.5%), classified as boninite. Phanerozoic boninitic rocks occur exclusively in convergent margin settings and are rarely seen in Precambrian terrains. In this respect, occurrence of such rocks in Bastar craton may have important tectonic implications. This communication presents preliminary results on petrological and geochemical characteristics of these high-Mg mafic dykes.

*For correspondence. (e-mail: rajeshgeolbhu@yahoo.com)

THE Archaean Bastar craton comprises a vast tract of granitoids and mafic rocks of different petrological characteristics, supracrustal rocks and unmetamorphosed late Proterozoic sedimentaries[1–3]. The Bastar craton is bounded by NW–SE trending Mahanadi and Godavari rifts, ENE–WSW trending Narmada–Son rift and Eastern Ghats Mobile Belt[2] (Figure 1). These rifts are supposed to be ancient and probably existed since the Archaean time[4,5]. Existence of these rifts in central Indian craton since the Archaean time and regional geology, including metamorphism[3] and distinctive sedimentary records[6,7], suggest the existence of a stable continental rift environment in the Central Indian craton[8–13].

Mafic igneous rocks of Precambrian age are a common feature that occurred in almost all the Archaean cratons of the globe, including the Indian Shield and provided valuable information on the role of crustal evolution[2,14–16]. The Archaean Bastar craton manifested several episodes of mafic magmatism, which include mafic dyke swarms and mafic volcanics[6,8–13]. Although few earlier workers have reported mafic dykes of different nature and age in this craton, little was known about their geochemical characteristics before the work done by the present authors. We have recognized two distinct mafic dyke swarms of sub-alkaline nature in the southern part of the Bastar craton[8,13]. The middle Archaean older set of sub-alkaline mafic dykes is metamorphosed under amphibolite facies conditions and shows low-Ti (~ 1.7%), low-Fe and moderate-Mg (~ 6%) geochemical characteristics. On the other hand, the younger set, of sub-alkaline mafic dykes which is Palaeoproterozoic (~ 1.8 Ga) in age, is fresh and shows comparatively different geochemical

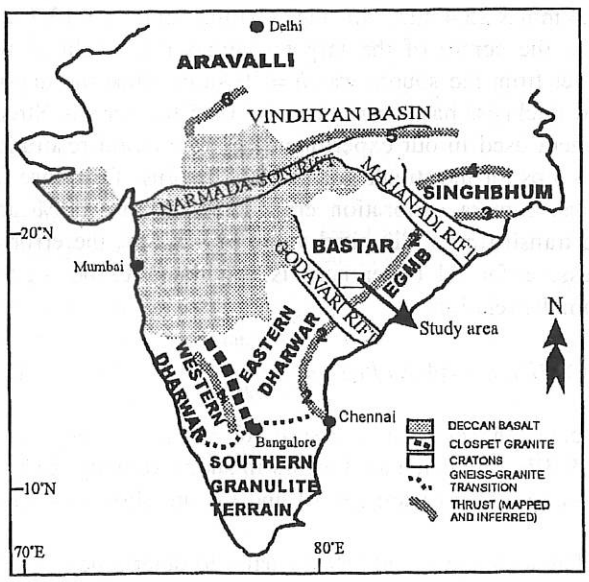

Figure 1. Major cratons and structural features of India[2]. Major structural features are: 1, Small thrusts in western Dharwar craton; 2, Eastern Ghats front; 3, Sukinda; 4, Singhbhum; 5, Son Valley, and 6. Great Boundary fault. EGMB, Eastern Ghats Mobile Belt.